batteries

MDPI

Article

Urea-Based Deep Eutectic Solvent with Magnesium/Lithium Dual Ions as an Aqueous Electrolyte for High-Performance Battery-Supercapacitor Hybrid Devices

Hsin-Yen Tsai [1], Munusamy Sathish Kumar [1], Balaraman Vedhanarayanan [1,2], Hsin-Hui Shen [3] and Tsung-Wu Lin [1,*]

[1] Department of Chemistry, Tunghai University, No.1727, Sec.4, Taiwan Boulevard, Xitun District, Taichung City 40704, Taiwan
[2] Department of Applied Chemistry and Biotechnology, Graduate School of Engineering, Chiba University, 1-33 Yayoi-cho, Inage-ku, Chiba 263-8522, Japan
[3] Department of Materials Science and Engineering, Monash University, Clayton, VIC 3800, Australia
* Correspondence: twlin@thu.edu.tw

Abstract: A new deep eutectic solvent (DES) made from urea, magnesium chloride, lithium perchlorate and water has been developed as the electrolyte for battery-supercapacitor hybrid devices. The physicochemical characteristics of DES electrolytes and potential interactions between electrolyte components are well analyzed through electrochemical and spectroscopic techniques. It has been discovered that the properties of DES electrolytes are highly dependent on the component ratio, which allows us to engineer the electrolyte to meet the requirement of the battery application. Perylene tetracarboxylic di-imide and reduced graphene oxide ha ve been combined to produce a composite (PTCDI/rGO) that has been tested as the anode in DES electrolyte. This composite shows that the capacitive contribution is greater than 90% in a low scan rate, resulting in the high rate capability. The PTCDI/rGO electrode exhibits no sign of capacity degradation and its coulombic efficiency is close to 99% after 200 cycles, which suggests excellent reversibility and stability. On the other hand, the electrochemical performance of lithium manganese oxide as the cathode material is studied in DES electrolyte, which exhibits the maximum capacity of 76.5 mAh/g at 0.03 A/g current density. After being successfully examined in terms of electrode kinetics, capacity performance, and rate capability, the anode and cathode materials are combined to construct a two-electrode system with DES electrolyte. At a current density of 0.03 A/g, this system offers 43.5 mAh/g specific capacity and displays 55.5% retention of the maximum capacity at 1 A/g. Furthermore, an energy density of 53 Wh/kg is delivered at a power density of 35 W/kg.

Keywords: hybrid supercapacitor; deep eutectic solvent; urea; organic electrode; magnesium/lithium dual ions

check for updates

Citation: Tsai, H.-Y.; Kumar, M.S.; Vedhanarayanan, B.; Shen, H.-H.; Lin, T.-W. Urea-Based Deep Eutectic Solvent with Magnesium/Lithium Dual Ions as an Aqueous Electrolyte for High-Performance Battery-Supercapacitor Hybrid Devices. *Batteries* **2023**, *9*, 69. https://doi.org/10.3390/batteries9020069

Academic Editor: Seiji Kumagai

Received: 28 November 2022
Revised: 9 January 2023
Accepted: 16 January 2023
Published: 18 January 2023

Copyright: © 2023 by the authors. Licensee MDPI, Basel, Switzerland. This article is an open access article distributed under the terms and conditions of the Creative Commons Attribution (CC BY) license (https://creativecommons.org/licenses/by/4.0/).

1. Introduction

High-performance rechargeable batteries are critical for expanding the use of intermittent renewable energy sources such as wind and solar power. Li-ion batteries (LIBs), in particular, have achieved enormous commercial success in portable devices and electric vehicles due to their high energy density and great lifespan. For grid-level stationary applications, LIBs with flammable organic electrolytes may raise huge safety concerns especially if the battery facility is quite big, similar to the dimensions of typical shipping containers [1,2]. In addition to energy density, one of the primary parameters for assessing practical batteries is the levelized energy cost across the device's cycle life [2,3]. In that case, the creation of alternative energy storage technologies has been rapidly advancing because of the limited lithium reserves in the crust and the high production costs of LIBs [4–6]. Multivalent metal-ion batteries such as Mg^{2+} [7,8], Zn^{2+} [9,10], Ca^{2+} [11,12] and Al^{3+} [13,14],

have received a lot of attention because of their high natural abundance, good chemical stability, wide distribution, environmental friendliness and low cost, [15,16]. Compared with monovalent metal-ion batteries, multivalent metal-ion batteries can transmit more electrons per time and provide more energy densities [7]. During the last two decades, magnesium-ion batteries (MIBs) stand out among other multivalent metal-ion batteries for several reasons including their dendrite-free nature, plenty of reserves in the crust of the earth (2.9%), large theoretical volumetric capacity (3833 mAh cm^{-3}), and small reduction voltage (−2.37 V compared with conventional hydrogen electrode) [17]. However, current MIBs still face numerous challenges due to the huge polarization effect and slow solid-state diffusion brought on through the robust electrostatic interaction among Mg ions and the host [18–20].

Organic electrodes are recently attracted a lot of attention because of their intrinsic benefits over traditional inorganic electrodes, such as their rotational flexibility and access to numerous natural resources [21–23]. Additionally, compared to a few inorganic electrodes that perform irreversibly, the organic electrodes exhibit a more capable potential for multivalent-ion storage since their ion storage performances depend on slight conversion processes between the ionic charge carriers and the functional groups [24]. Organic electrodes may therefore be suitable for high-performance MIBs, albeit few related studies have been published yet [25,26]. In light of their affordability and low carbon dioxide emissions during their synthesis, redox organic compounds have been proposed as possible substitute electrode materials for transition-metal-oxide in the battery field [27]. The future development of high-capacity organic electrodes holds great promise due to the chemical variety of organic redox compounds and their lightweight, whereas the theoretical maximum capacity of conventional electrodes based on transition metal oxides has nearly been reached and still there is a small space remains for further improvement [25]. Numerous organic electrode materials, such as conducting polymers [28,29], organic carbonyls [29], and organic radicals [30] have also been developed. Early redox-active organic species had poor cyclic stability and rate capability owing to their high solubility and low conductivity in liquid electrolytes [31,32]. To increase the conductivity of organic compounds, mixing a high-conductive carbonaceous substrate such as carbon nanotubes [33–35] and graphene [36], with active materials is a widespread strategy. Furthermore, organic molecules' structural layout and functional engineering also significantly influence how well they operate electrochemically. For instance, electrolyte ions can easily acquire access to active sites in organic molecules with thin and flexible architectures. It is essential to select the proper electrolyte system to prevent the organic electrode from dissolving. As promising electrolytes for aqueous metal-ion batteries and supercapacitors, deep eutectic solvents (DES) and water-in-salt (WIS) have recently grabbed attention [37,38]. Recently, WIS electrolyte has drawn a lot of attention as a novel aqueous electrolyte because it combines the advantages of aqueous electrolytes with the broad electrochemical stability window (ESW) of nonaqueous electrolytes. Similar to conventional aqueous electrolytes, the WIS electrolyte has the benefits of less toxicity, high safety, and great environmental friendliness [39,40]. In the case of WIS electrolytes, the formation of high-concentration solutions necessitates the use of highly soluble salts. As a result, the price of salt has a significant impact on the practical applicability of WIS in energy storage devices [41]. On the other hand, DES is a multi-component system where appropriate hydrogen bond acceptors and donors form a complex. The DES exists in four different types, depending on whether quaternary ammonium salts are combined with metal chloride (type I), metal chloride hydrate (type II), hydrogen bond donor (type III), or metal chloride hydrate with hydrogen bond donor (type IV) [42]. The melting point, viscosity, and ionic conductivity of DES are governed by intermolecular forces such as hydrogen bonds, interactions of Lewis acid-base, and the Van der Waals force. DES is broadly acknowledged as a new class of ionic liquid analogs due to low vapor pressure, high thermal stability, broad ESW, and tunability. DES electrolytes can overcome the shortcomings of other electrolytes, including the toxicity and safety concerns of organic electrolytes, the high cost of ionic liquids, the limited ESW of aqueous

electrolytes, etc [43,44], therefore, they have become the focus of recent studies in the field of energy storage.

In this work, the novel urea-based DES has been prepared as an aqueous electrolyte of MIBs, which exhibits a significant cost advantage over WIS. The physical properties of DES electrolytes and the possible interaction between electrolyte components are systematically investigated. Additionally, the composite perylene tetracarboxylic di-imide with reduced graphene oxide (PTCDI/rGO) has been investigated as the anode for MIBs in DES electrolytes. This organic anode's electrode capacity functioning, kinetics, and charge storage mechanism have all been examined. To further demonstrate the practical application of DES electrolyte, PTCDI/rGO as the anode is coupled to lithium manganese oxide (LMO) as the cathode in the tests of two electrode systems. This system distributes 43.5 mAh/g at 0.03 A/g and retains 55.5% of the maximum specific capacity at 1 A/g.

2. Materials and Methods

2.1. Preparation of DES Electrolyte

In the argon-filled glove box, urea ($CO(NH_2)_2$, 99%, Showa chemical Ltd.) and anhydrous magnesium chloride ($MgCl_2$, 99%, Alfa Aesar) were first mixed in various molar ratios of x: 1 (x = 5, 6, and 7). However, a particular amount of water was added to the above precursors and the resulting mixture was agitated at 80 °C for two hours. The resultant liquid is represented by the notation W(y)-Mg-DES(x), where "y" is the molar ratio of the water to the $MgCl_2$ (y= 4, 5, and 6). For the DES with dual cations (abbreviated as W(y)-Mg/Li-DES(x)), the molar ratio of $MgCl_2$ to lithium perchlorate ($LiClO_4$, 95%, Alfa Aesar) was 20:1.

2.2. Physicochemical Characterizations of Electrolytes

To conduct burning tests, the filter paper (3 cm^2) has been drenched in the various electrolytes (40 μL) and then ignited using the torch. Anti-freeze properties were observed by immersing different DES electrolytes in ethanol at a low temperature controlled by an immersion cooler (CC-100, Neslab). Raman analyses were carried out by using a Raman spectrometer (Horiba JY iHR550, LabSpec 5) with a 532 nm laser. Infrared spectra were measured on a Fourier transform Infrared (FTIR) spectrometer (Spectrum 100, PerkinElmer). To identify the DES electrolytes ESW value, carbon cloth (1 cm^2), graphite rod, and Ag/AgCl electrode were used as working, counter and reference electrodes, respectively, in the three-electrode system. The Linear sweep voltammetry (LSV) was carried out at 1 mV s^{-1} scan rate using CH Instruments 635A. The ESW of DES was determined by the current density threshold of 0.2 mA cm^{-2}.

2.3. Material and Electrochemical Characterizations of PTCDI/rGO Composite

The synthetic procedures of the PTCDI/rGO composite were followed according to our previous work [45]. The microstructures and morphologies were observed using scanning electron microscopy (SEM; JEOL JSM-6510) and transmission electron microscopy (TEM; JEOL JSM-2100F) mounted with an energy-dispersive X-ray spectrometer (EDX). The phase and composition were analyzed with the help of X-ray powder diffractometer (XRD, Rigaku Miniflex).

For the electrode preparation, the slurry was made by mixing N-methyl pyrrolidone (C_5H_9NO, 97%, Wako) with the powder containing an active material, carbon black, and polyvinylidene difluoride with the weight ratio of 7:2:1. Next, the slurry was evenly coated onto the carbon cloth (Cetech, Taichung, Taiwan, 10 × 10 mm^2) and then dried at 40 °C for overnight. The loaded mass of active materials on the electrode surface was determined to be 1.2 mg/cm^2. The cyclic voltammetry (CV), galvanostatic charge-discharge (GCD), and cyclic stability tests were conducted to study the electrode performance in DES electrolytes using CH Instruments 635A.

3. Results and Discussion

3.1. Characterization of Electrolytes

The urea concentration in the DES electrolyte has been varied to optimize electrolyte properties. The LSV tests were carried out for different electrolytes to determine the ESW values as shown in Figure 1a. The ESW values for the electrolytes of W(6)-Mg-DES(5), (6), and (7) are 2.92, 2.89, and 2.72 V, respectively, Furthermore, it is discovered that as the urea ratio rises, the ionic conductivity increases as well. On the other hand, the characteristics of DES electrolytes are significantly influenced by the water content. When the $H_2O/MgCl_2$ molar ratio is increased from 4 to 6 in the example of Mg-DES(7), the ionic conductivity rises from 0.97 to 4.33 mS/cm, while the ESW falls from 3.29 to 2.72 V. It has been reported that the ESW range is highly sensitive to the water content in the DES electrolyte and the free water fraction is one of the major key factors which affect the electrochemical stability of electrolytes [46]. In our hybrid DES system, the water molecules likely interact with urea and metal salts through the strong hydrogen bonds, which leads to the suppression of water decomposition. However, some free water molecules may be present in the electrolyte with higher water content, which reduces ESW value. Although DES has a smaller ionic conductivity than previously reported WIS electrolytes, the former shows a comparable ESW value to the latter [39,47]. The impact of second metal ions on DES performance is also investigated. Ionic conductivity decreases when more Li salt is added to the DES electrolyte, as illustrated in Figure 1b. Ionic conductivity and ESW value both increase when the Li salt level drops. The physical status of DES electrolytes with various urea contents is examined as seen in Figure 1c. While DES electrolytes are resistant to freezing, it has been reported that 1 M $MgSO_4$ electrolyte freezes at −20 °C. It is noteworthy that W(6)-Mg-DES(7) exhibits greater fluidity than W(6)-Mg-DES(5). Additionally, the fluidity of W(6)-Mg-DES(7) is unaffected by the addition of Li salt. The ionic conductivity of W(6)-Mg/Li-DES(7) is significantly decreased from 3.88 to 0.865 mS cm^{-1} when the temperature is changed from 25 to −10 °C. This result is attributed to the high viscosity of 4067 mPa·s at the lower temperature. The burning test of filter paper soaked in DES electrolytes was carried out to evaluate the safety of the DES electrolytes. It should be mentioned that every DES electrolyte exhibits a remarkable flame-retardant behavior (in the lower right corner of Figure 1c). Various DES electrolytes are analyzed using Raman spectroscopies to know a better understanding of the interaction between DES components. Figure 1d exhibits the Raman spectra of various DES, H_2O, and Urea. The CO symmetric stretching of urea is usually observed at 1532 cm^{-1} [48], whereas the same peak is shifted towards a higher wavenumber (known as blue shift) for DES electrolytes. The CO peak is located at 1590, 1596, and 1597 cm^{-1} for W(6)-Mg-DES(5), W(6)-Mg-DES(7), and W(6)-Mg/Li-DES(7), respectively. Similarly, NH_2 symmetric deformation of urea was observed at 1636 cm^{-1}, which is also shifted to 1661, 1662, and 1666 cm^{-1} for the aforementioned hybrid DES electrolytes. Furthermore, it is noted that the N-H stretching mode of urea is observed at a higher wavenumber of 3350 cm^{-1} and this mode also shifts to 3367, 3370, and 3375 cm^{-1} for hybrid DES electrolytes. When water molecules are added to DES to generate hybrid DES, the peaks shift to a higher wavenumber. This occurs as a result of the weakening of the hydrogen bonds (via N-H and CO groups) among the individual urea molecules and, at the same time, the increased interactions with water and metal salts. Additionally, the nonappearance of a broad water peak suggests that H_2O molecules are bonded to DES constituents. It is important to notice that the W(6)-Mg/Li-DES(7) electrolyte exhibits a more blue shift of the N-H mode towards the higher wavenumber in contrast to other electrolytes because the addition of Li ions may further weaken the hydrogen bonds in urea molecules [49,50].

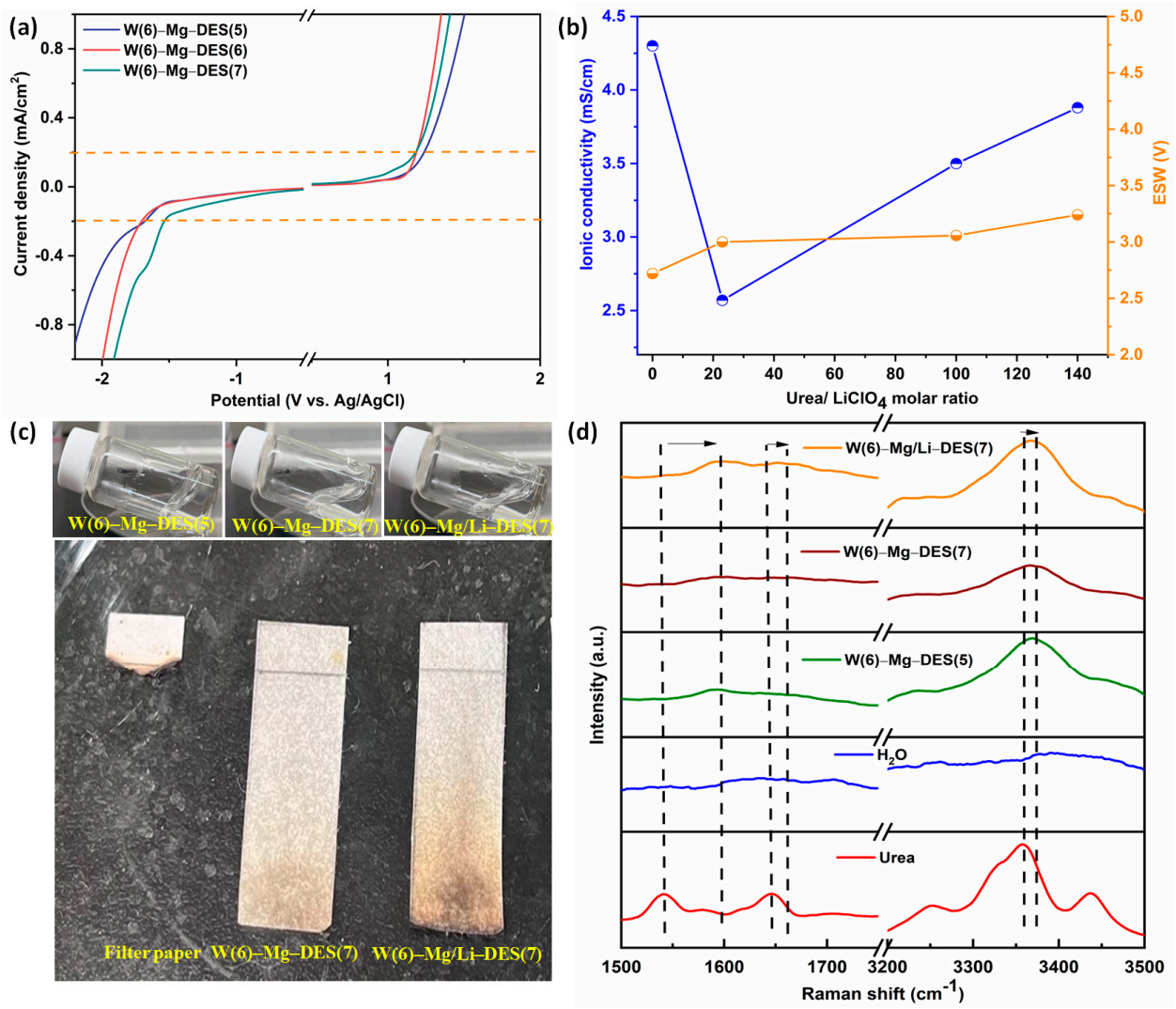

Figure 1. (**a**) LSV curves for different DES electrolytes. (**b**) Ionic conductivity and ESW value of DES electrolyte with different urea/$LiClO_4$ molar ratios. (**c**) Freezing resistance and flame-retardant test of the various electrolytes. (**d**) Raman spectra for different DES electrolytes.

3.2. Material Characterization of the Composite PTCDI/rGO and Pure PTCDI

Figure 2a shows the monoclinic structure of the PTCDI/rGO and PTCDI samples, that has a space group of P21/n. The significant peaks occur at 10°, 12°, 25°, 27.1°, and 30.4° are the diffraction of the crystalline planes (011), (020), ($\bar{1}$12), ($\bar{1}$22) and ($\bar{1}$32), respectively [51]. Notably, the XRD pattern of the sample PTCDI with a core of aromatic perylene demonstrates several sharp peaks caused by diffraction but the addition of rGO into the PTCDI sample does not affect its crystalline nature. The FTIR spectra of the PTCDI/rGO composite and PTCDI substance are shown in Figure 2b. The IR band at around 1681 cm^{-1} is present in both PTCDI and the corresponding composite due to the stretching vibration of C=O [52]. The perylene ring stretching vibration is observed at 1573 cm^{-1}. While two peaks for aromatic -CH stretching vibrations are located at 2857 and 3040 cm^{-1}, respectively, the stretching vibration of -C-N- is observed at 1361 cm^{-1}. Furthermore, a peak at 3155 cm^{-1} is attributed to the N-H stretching vibration. These results also clearly indicate that the addition of the rGO sample into PTCDI does not disturb its original structure. The SEM image of PTCDI/rGO aggregates is displayed in Figure 2c. PTCDI nanoribbons have an aspect ratio of approximately 250:1500 nm. Organic materials' structures are typically determined by interactions between functional groups within a molecule. Strong stacking interactions between aromatic perylene cores in PTCDI lead

to an ordered arrangement that promotes the formation of a ribbon kind of structure. A ribbon-such as PTCDI is maintained in the PTCDI/rGO composite, and all these ribbons are dispersed across the rGO substrate to produce flake-like aggregates with high surface area and potent interfacial interactions. This may enhance the electrochemical performance of composite than pure PTCDI due to the improvement of electric conductivity [52]. The ultra-thin nature of PTCDI nanoribbons is highly transparent observed in TEM images, which permits magnesium ions to swiftly and reversible intercalations into the interior of the PTCDI throughout the charge-discharge cycles (Figure 2d). The elements C, N, and O are evenly distributed throughout the composite, as shown by the elemental mapping data.

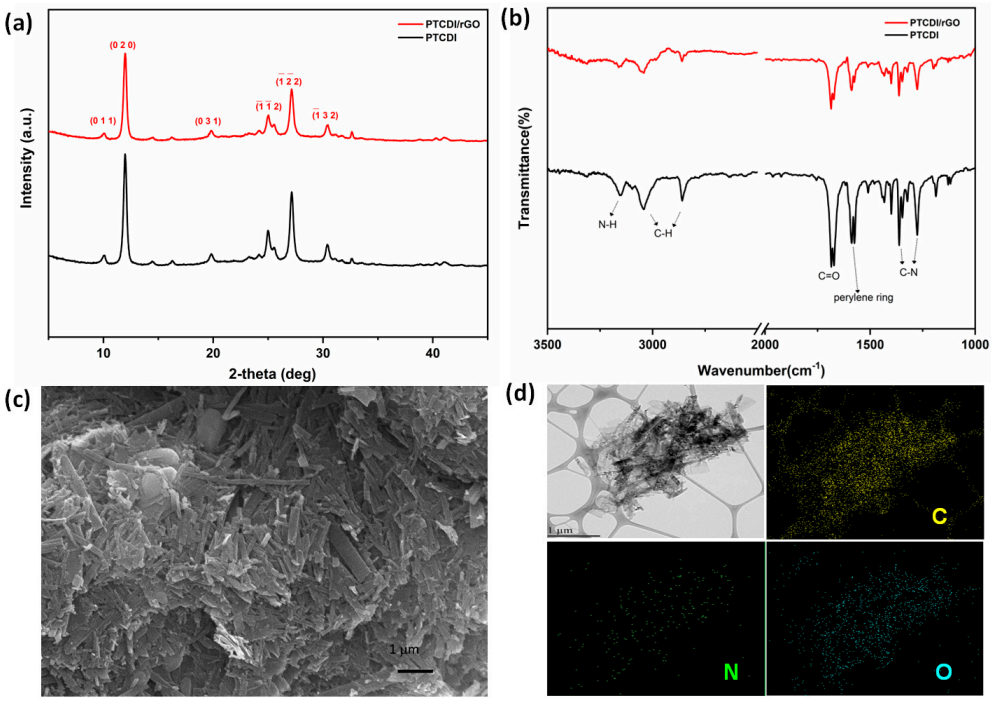

Figure 2. (**a**) XRD patterns and (**b**) FTIR spectra of PTCDI and PTCDI/rGO. (**c**) SEM image of the PTCDI/rGO. (**d**) TEM image of PTCDI/rGO and its corresponding mapping images for C, N, and O elements.

3.3. Electrochemical Performances of the PTCDI/rGO Anode and LMO Cathode in the Electrolyte of W(6)-Mg/Li-DES(7)

As illustrated in Figure 3a, CV analysis of the composite PTCDI/rGO was carried out at various scan rates to recognize the energy storage mechanism of the electrode. PTCDI/rGO shows the oxidation peaks at approximately −0.69 and −0.12 V, and the reduction peaks at −0.94 and −0.35 V. During the electrochemical investigation, the carbonyl groups reversible enolization in the sample PTCDI is responsible for the two pairs of observed redox peaks [51]. Furthermore, the capacitive behavior of rGO may be hidden behind these peaks. These redox peaks move noticeably with increasing sweep rates, demonstrating rapid reaction kinetics while the charge storage. The electrode kinetics of the PTCDI/rGO composite were investigated using Equation (1).

$$i_p = a\, v^{\,b} \ldots\ldots\ldots\ldots \quad (1)$$

where i_p is the current density, v is the scan rate, "a" and "b" is a constant. When b ≈ 0.5 proposes that diffusion-controlled process (C1, battery-like behavior) is dominant. On the other hand, b ≈ 1.0 indicates that the surface-controlled process (C2, pseudocapacitive behavior) plays the primary role. Figure 3b shows that the b values of peaks 1, 2, 3, and 4 are 1.00, 0.86, 0.76, and 0.94, indicating that the C1 and C2 processes are combined. In order to further quantify the capacitive contribution, the current density (i) at a given volt-

age (V) can be split into two components, with k_1v representing the contribution controlled by capacitance and $k_2v^{1/2}$ representing the diffusion-controlled process as presented in Equation (2) [53].

$$i = k_1v + k_2v^{1\backslash 2} \ldots\ldots\ldots\ldots \quad (2)$$

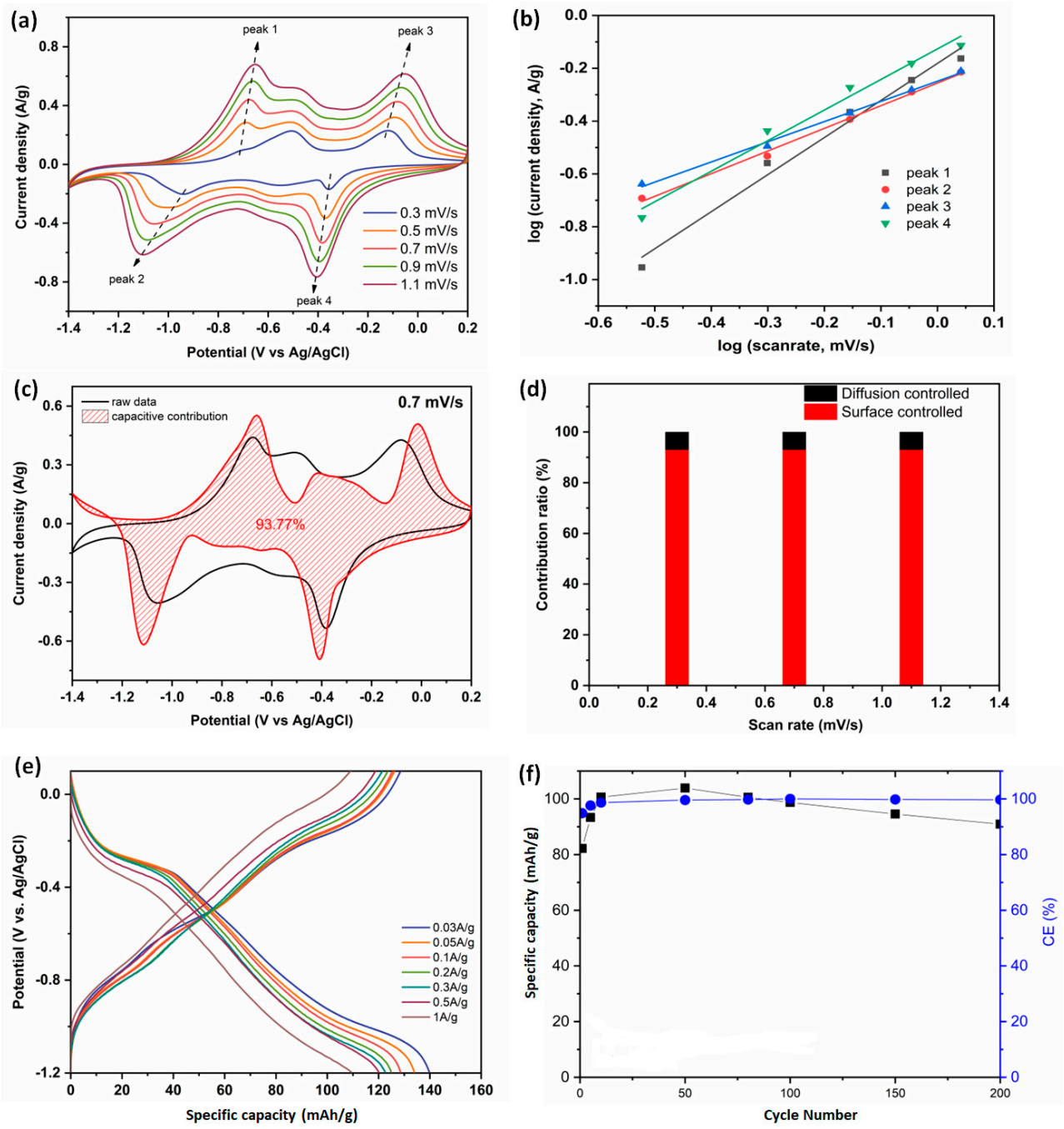

Figure 3. (**a**) The CV curves of PTCDI/rGO in W(6)–Mg/Li–DES(7) electrolyte with different scan rates. (**b**) The corresponding log *i* vs. log *v* plots with different redox states. (**c**) Capacitive contribution in CV curve for the composite electrode at 0.7 mV/s. (**d**) Bar chart showing the contribution ratio at different scan rates. (**e**) GCD curves of the PTCDI/rGO electrode with different current densities. (**f**) Stability test of PTCDI/rGO electrode at the current density of 2 A/g.

The capacitance contribution in the CV curve at a scan rate of 0.7 mV/s is clearly shown in Figure 3c. Figure S1 provides the additional CV curves with various scan rates.

In Figure 3d, the bar chart clearly reveals that the PTCDI/rGO electrode exhibits more than 90 % of capacitive contribution even at a low scan rate, which reflects the high-rate capability. Figure 3e shows the GCD curves of the composite electrode with different current densities ranging from 0.03 to 1 A/g. It is worth noting that PTCDI/rGO electrode possesses 139.8 mAh/g at 0.03 A/g and still maintains 78.2 % of maximum capacity even at the higher current density of 1 A/g. To better understand the superiority of rGO addition, the electrochemical performance of pure PTCDI was also evaluated in W(6)-Mg/Li-DES(7) electrolyte as illustrated in Figure S2. In a current density of 0.03 A/g, the PTCDI electrode displays a specific capacity of 118.7 mAh/g and retains 73% of its maximum capacity. As a result, it is well established that PTCDI/rGO electrode performs better than the pure PTCDI electrodes, which recommends that the addition of rGO improves charge transfer in the electrode [45]. The measured specific capacity, coulombic efficiency, and the rate capability of PTCDI/rGO electrode in W(6)-Mg/Li-DES(7) electrolyte at different current densities are given in Table S1. Figure 3f displays the specific capacity and coulombic efficiency as a function of cycle numbers. The first few rises in specific capacity may be due to the electrode activation during the cycling process. The specific capacity of the composite is 91 mAh/g even after 200 cycles, which shows no sign of electrode degradation. More importantly, the coulombic efficiency of the electrode is almost 99 % during the stability test, which implies the great reversibility of the electrode and excellent stability of the electrolyte.

The prominent ions that interact with PTCDI/rGO should be identified because W(6)-Mg/Li-DES(7) electrolyte contains two different cations. The PTCDI/rGO electrode was tested in a three-electrode system with various electrolytes, including 1M LiCl, W(6)-Mg-DES(7), and W(6)-Mg/Li-DES(7), as shown in Figure S3a–f. Although the potentials of redox peaks depend on the type of used electrolyte, the capacities of the PTCDI/rGO electrode in 1M LiCl are similar to those in W(6)-Mg-DES(7). It is noteworthy that the composite electrode in DES electrolyte exhibits better coulombic efficiency and a wider potential window when compared to the traditional 1 M LiCl electrolyte. This result suggests that the use of DES electrolytes prevents the occurrence of hydrogen evolution during the discharge process in the electrode. Furthermore, the addition of Li salt into W(6)-Mg-DES(7) does not significantly change the electrochemical performance of the PTCDI/rGO electrode, which indicates Mg ions are the dominant ions to interact with the composite electrode. As shown in Figure S3c,e, the redox peaks recorded from the two electrolytes are well overlapped, which further supports the above result.

As shown in Figure 4, the electrochemical tests of LMO as cathode material were carried out in W(6)-Mg/Li-DES(7) electrolyte. In the CV curves of LMO with different scan rates (0.3–1.1 mV/s), the redox peaks are observed at 0.85, 0.75, 1.02, and 0.90 V (vs. Ag/AgCl) for peaks 1 to 4, respectively. In the cathodic scan, the Li ions occupy half of the tetrahedral '8a' sites of the $LiMn_2O_4$ spinel crystal structure, creating the first reductive CV peak (so-called stage II). When the potential continues decreasing, the other half of the '8a' sites are filled with Li ions, which corresponds to the second reductive CV peak (so-called stage I). In the anodic scan, the deintercalation of Li-ions out of $LiMn_2O_4$ leads to two oxidative CV peaks [54,55]. The electrode kinetics of LMO material is also examined. As shown in Figure 4b, the calculated b values for peaks 1 to 4 are 0.56, 0.64, 0.54, and 051, respectively. According to the b values, the energy storage mechanism of the LMO electrode mainly involves a diffusion-controlled process. As shown in Figure 4c and Figure S4, LMO exhibits only 37% of capacitive contribution even at a higher scan rate of 1.1 mV/s, which reflects the battery-like behavior. As shown in the GCD curve (Figure 4d), LMO exhibits two obvious plateaus in the potential range from 0.5 to 1 V, which are consistent with the positions of their redox peaks in CV curves. The LMO cathode provides a maximum capacity of 76.5 mAh/g at 0.03 A/g which retains 12 % of maximum capacity as well as 97.6 % of coulombic efficiency at 1 A/g. The measured specific capacity, coulombic efficiency, and rate capability of LMO electrode in W(6)-Mg/Li-DES(7) electrolyte at different current densities are given in Table S2. To clarify the dominant ion for the intercalation of the

electrode, the LMO performance was further analyzed in the electrolyte of W(6)-Mg-DES(7). As shown in Figure S5 and Table S3, the maximum specific capacity of 18.6 mAh/g is observed at 0.03 A/g, which is significantly lesser than the capacity measured in W(6)-Mg/Li-DES(7) electrolyte. This result is strong evidence that the LMO performance is highly sensitive to the presence of Li salt in the electrolyte. Another cathode material, lithium iron phosphate ($LiFePO_4$, LFP), was also tested in W(6)-Mg/Li-DES(7) electrolyte. As shown in Figure S6 and Table S4, the obtained specific capacity of LFP material is about 110 mAh/g at 0.03 A/g and shows 23.6 % retention of maximum capacity as well as 95.9 % coulombic efficiency at the current density of 1 A/g. The LFP electrode exhibits great reversibility and electrochemical efficiency during the charge-discharge processes, which suggests the excellent compatibility of W(6)-Mg/Li-DES(7) electrolytes with different electrode materials.

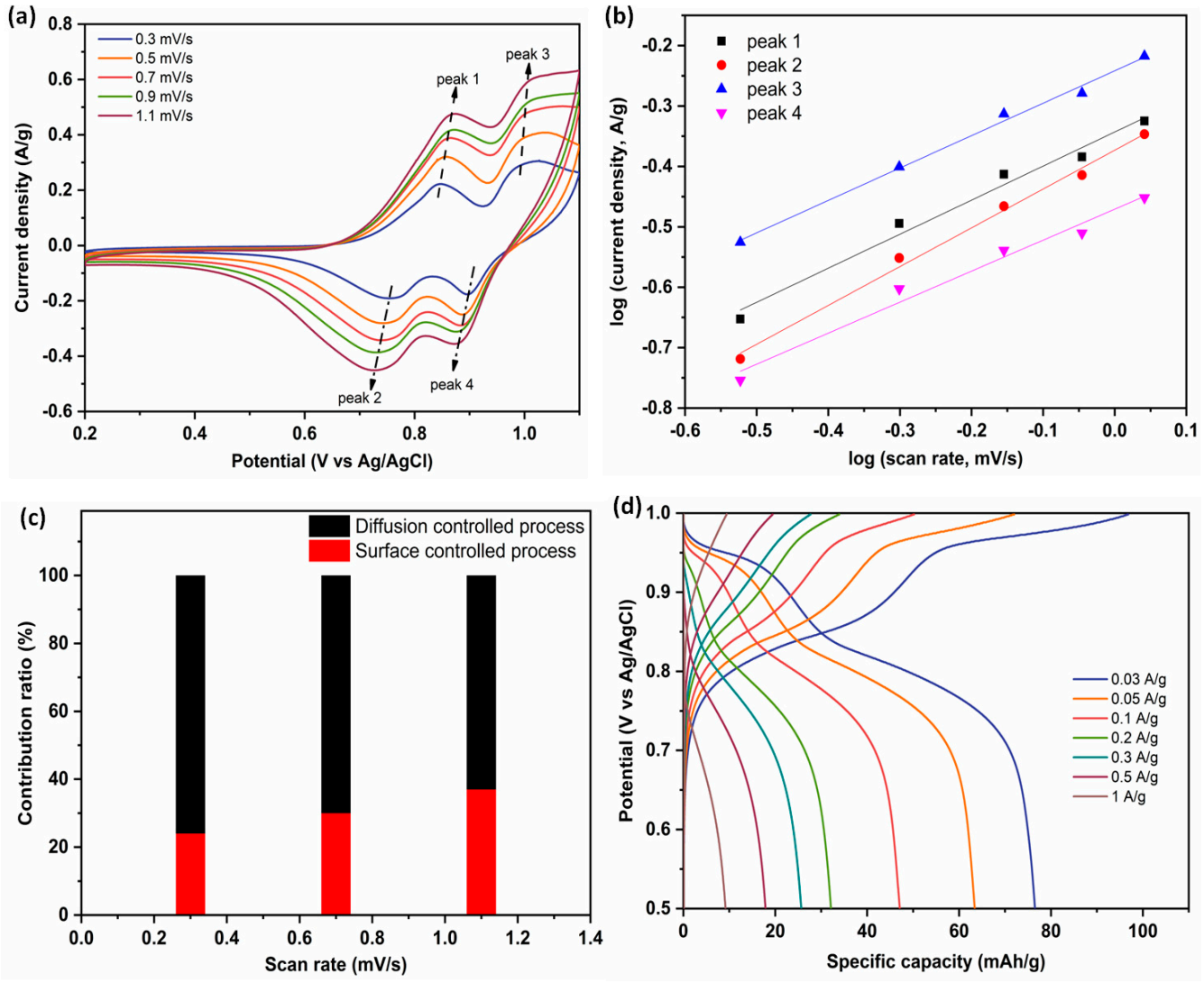

Figure 4. (**a**) CV curves, (**b**) the plot of log *i* vs. log *v*, (**c**) bar chart showing the contribution ratio and (**d**) GCD curves of the LMO cathode in W(6)–Mg/Li–DES(7) electrolyte.

3.4. Two Electrode Measurements

In order to demonstrate the practical use of DES electrolytes for MIBs, two electrode measurements were carried out using PTCDI/rGO composite as the anode with LMO as the cathode. The total mass loading of the active materials is 1.9 mg after considering the capacity balance between the two electrodes. Figure 5a shows the CV curves of two electrode systems where the CV peaks in the 2nd and 3rd cycle look similar but their

intensities are greater than those in the first cycle, indicating that the reactions taking place throughout the cycling process could not affect the electrode materials' reactivity [56]. Furthermore, the obvious oxidative peaks emerge at 1.16, 1.39, and 2.01 V, attributed to the deintercalation of Li^+ from the LMO electrode and the intercalation of Mg^{2+} into the PTCDI/rGO. On the other hand, the reductive peaks appear at 0.86, 1.27, and 1.63 V, which may be the result of the extraction of Mg^{2+} ions from the anode and the insertion of Li^+ ions into the cathode. The above result implies the reliable reversible property of MIBs. As shown in Figure 5b, the GCD experiments at various current densities demonstrate that the system can be operated in a wide working voltage window between 0.01 to 2.20 V, and also it can deliver 43.5 mAh/g maximum specific capacity at a measured current density of 0.03 A/g. Furthermore, 55.5 % of the maximum specific capacity has remained at 1 A/g, which indicates a great rate capability. The calculated specific capacity and coulombic efficiency of the two electrode system is summarized in Table S5. As shown in Figure 5c, our system achieves the maximum energy density of 53 Wh kg^{-1} at the power density of 35 W kg^{-1} and still delivers 26 Wh kg^{-1} at 1042 W kg^{-1}, which is comparable to the previously reported aqueous MIB devices (Table S6). The cyclic stability and coulombic efficiency of the two-electrode system are also investigated at the current density of 0.2 A/g. It is observed from Figure 5d that the capacity gradually decreases with increasing cycle number. The poor capacity retention may be attributed to the instability of the LMO electrode. According to the previous reports, the degradation of LMO crystal structure and the dissolution of Mn into aqueous Li_2SO_4 or $LiNO_3$ solution are typically the main cause of poor cycling performance [57,58]. This problem may be further solved by changing other cathode materials, which is our future task.

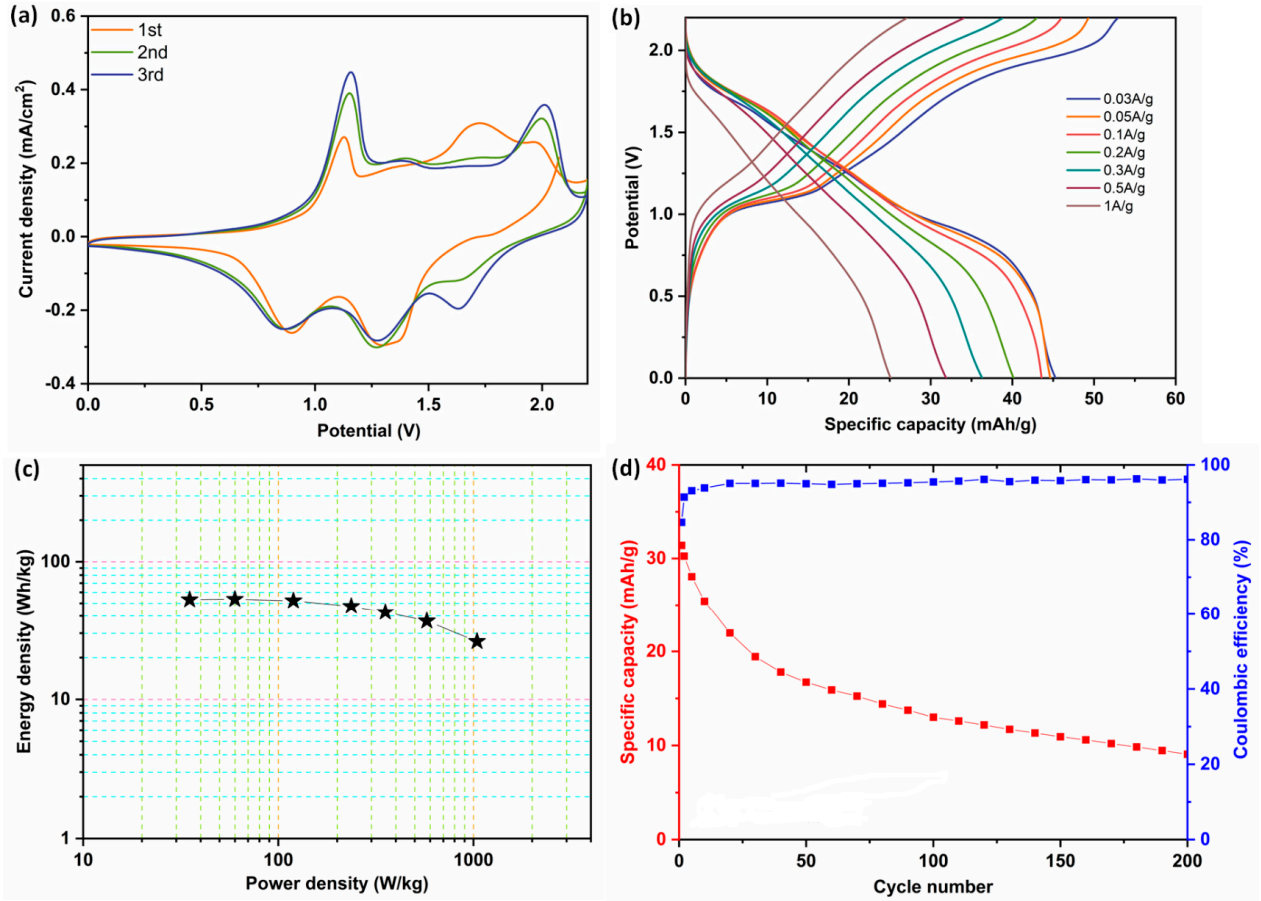

Figure 5. (**a**) CV curves, (**b**) GCD profiles, (**c**) Ragone plot, and (**d**) Cyclic stability tests of two electrode systems consisting of PTCDI/rGO, LMO, and W(6)–Mg/Li–DES(7) as the anode, cathode, and electrolyte, respectively.

4. Conclusions

The novel urea-based deep eutectic solvent has been designed as an aqueous electrolyte for MIBs. The studies of LSV, ionic conductivity, anti-freezing, and flame-retardant properties demonstrate the exceptional qualities of DES electrolytes. Raman spectroscopies are used to examine DES electrolytes in order to better understand how DES components interact with one another. The hydrothermally synthesized PTCDI/rGO composite is used as the anode for MIBs. According to XRD and FTIR analyses, the PTCDI sample's crystalline nature and original structural integrity are unaffected by the addition of rGO. Due to the ultra-thin nature of PTCDI nanoribbons, magnesium ions can rapidly and reversibly penetrate deep into the interior of the material during the charge-discharge process. Furthermore, the ribbon-like structures are induced by the strong stacking interactions between aromatic perylene cores, and such ribbons are then spread throughout the substrate rGO to produce flakes-like aggregates with high surface area. According to CV and GCD experiments in W(6)-Mg/Li-DES(7), the energy storage mechanism of the PTCDI/rGO electrode mainly involves a pseudocapacitance-controlled process, which imparts excellent rate capability performance. For example, PTCDI/rGO exhibits 139.8 mAh/g at 0.03 A/g and still maintains 78.2 % of maximum capacity even in a higher current density of 1 A/g. Furthermore, the specific capacity of 91 mAh/g was attained even after 200 cycles at 2 A/g, which demonstrates the great cyclic stability of PTCDI/rGO. The electrochemical performance of the LMO cathode in the W(6)-Mg/Li-DES(7) electrolyte was also tested. In contrast to PTCDI/rGO, LMO electrode principally follows a battery-like energy storage mechanism. The electrode material LMO distributes the specific capacity of 76.5 mAh/g at 0.03 A/g and retains 12% of maximum capacity at 1 A/g. In order to demonstrate the practical application of MIB, the electrochemical performance of a two-electrode system consisting of a PTCDI/rGO anode and LMO cathode was examined in W(6)-Mg/Li-DES(7) electrolyte. The system shows the specific capacity of 43.5 mAh/g at a current density of 0.03 A/g and still retains 55.5% of the maximum capacity at 1 A/g. Furthermore, a high energy density of 53 Wh/kg is delivered at a power density of 35 W/kg, which is comparable to the previous MIB devices. These results clearly demonstrate that our DES electrolytes have great potential for the battery industry.

Supplementary Materials: The following supporting information can be downloaded at: https://www.mdpi.com/article/10.3390/batteries9020069/s1. Figure S1: CV curves with the capacitive contribution of PTCDI/rGO in W(6)-Mg/Li-DES(7) electrolyte at the different scan rates; Figure S2: CV and GCD curves of pure PTCDI measured in W(6)-Mg/Li-DES(7); Figure S3: CV and GCD curves of PTCDI/rGO measured in 1 M LiCl, W(6)-Mg-DES(7) and W(6)-Mg/Li-DES(7) electrolytes; Figure S4: CV curves with the capacitive contribution of the LMO electrode in W(6)-Mg/Li-DES(7) electrolyte at the different scan rates; Figure S5: CV and GCD curves of the sample LMO in W(6)-Mg-DES(7) electrolyte; Figure S6: CV and GCD curves of the LFP electrode in W(6)-Mg/Li-DES(7) electrolyte; Table S1: Electrochemical performances of PTCDI/rGO cathode in W(6)-Mg/Li-DES(7) electrolyte at different current densities; Table S2: Electrochemical performances of LMO cathode in W(6)-Mg/Li-DES(7) electrolyte at different current densities; Table S3: Electrochemical performances of LMO cathode in W(6)-Mg-DES(7) electrolyte with different current densities; Table S4: Electrochemical performances of LFP cathode in W(6)-Mg/Li-DES(7) electrolyte with different current densities; Table S5: Electrochemical performances of two electrode system with different current densities; Table S6: Performance comparison of aqueous MIBs with different electrolytes and electrodes [59–64].

Author Contributions: H.-Y.T.: Conceptualization, Methodology, Validation, Investigation, Data Curation, Writing—Reviewing and Editing, Visualization; M.S.K.: Methodology, Investigation, Validation, Data Curation, Writing—Reviewing and Editing; B.V.: Methodology, Validation, Reviewing and Editing, Visualization; H.-H.S.: Methodology, Validation, Reviewing and Editing; T.-W.L.: Conceptualization, Methodology, Validation, Resources, Writing—Reviewing and Editing, Visualization, Supervision. All authors have read and agreed to the published version of the manuscript.

Funding: This research was funded by National Science and Technology Council (NSTC 111-2113-M-029-001, 111-2918-I-029-001 and 111-2811-M-029-005).

Data Availability Statement: The data the supports the findings of this study are available in the supplementary material of this article.

Conflicts of Interest: The authors declare no conflict of interest.

References

1. Li, W.; Dahn, J.R.; Wainwright, D.S. Rechargeable Lithium Batteries with Aqueous Electrolytes. *Science* **1994**, *264*, 1115–1118. [CrossRef]
2. Dunn, B.; Kamath, H.; Tarascon, J.M. Electrical Energy Storage for the Grid: A Battery of Choices. *Science* **2011**, *334*, 928–935. [CrossRef]
3. Kundu, D.; Talaie, E.; Duffort, V.; Nazar, L.F. The Emerging Chemistry of Sodium Ion Batteries for Electrochemical Energy Storage. *Angew. Chem. Int. Ed.* **2015**, *54*, 3431–3448. [CrossRef]
4. Lu, T.; Zhang, Z.; Chen, B.; Dong, S.; Wang, C.; Du, A.; Wang, L.; Ma, J.; Cui, G. A superior electronic conducting tellurium electrode enabled high-rate capability rechargeable Mg batteries. *Mater. Today Energy* **2020**, *17*, 100450. [CrossRef]
5. Thackeray, M.M.; Wolverton, C.; Isaacs, E.D. Electrical energy storage for transportation-approaching the limits of, and going beyond, lithium-ion batteries. *Energy Environ. Sci.* **2012**, *5*, 7854. [CrossRef]
6. Wang, Y.; Yi, J.; Xia, Y. Recent progress in aqueous lithium-ion batteries. *Adv. Energy Mater.* **2012**, *2*, 830–840. [CrossRef]
7. Muldoon, J.; Bucur, C.B.; Gregory, T. Fervent Hype behind Magnesium Batteries: An Open Call to Synthetic Chemists-Electrolytes and Cathodes Needed. *Angew. Chem. Int. Ed.* **2017**, *56*, 12064–12084. [CrossRef]
8. Zhang, Z.; Cui, Z.; Qiao, L.; Guan, J.; Xu, H.; Wang, X.; Hu, P.; Li, S.; Zhou, X.; Dong, S.; et al. Novel Design Concepts of Efficient Mg-Ion Electrolytes toward High-Performance Magnesium-Selenium and Magnesium-Sulfur Batteries. *Adv. Energy Mater.* **2017**, *7*, 1602055. [CrossRef]
9. Wang, H.; Wang, M.; Tang, Y. A novel zinc-ion hybrid supercapacitor for long-life and low-cost energy storage applications. *Energy Storage Mater.* **2018**, *13*, 1–7. [CrossRef]
10. Wang, F.; Borodin, O.; Gao, T.; Fan, X.; Sun, W.; Han, F.; Faraone, A.; Dura, J.A.; Xu, K.; Wang, C. Highly reversible zinc metal anode for aqueous batteries. *Nat. Mater.* **2018**, *17*, 543–549. [CrossRef]
11. Wang, M.; Jiang, C.; Zhang, S.; Song, X.; Tang, Y.; Cheng, H.M. Reversible calcium alloying enables a practical room-temperature rechargeable calcium-ion battery with a high discharge voltage. *Nat. Chem.* **2018**, *10*, 667–672. [CrossRef]
12. Ponrouch, A.; Frontera, C.; Bardé, F.; Palacín, M.R. Towards a calcium-based rechargeable battery. *Nat. Mater.* **2016**, *15*, 169–172. [CrossRef]
13. Yang, H.; Li, H.; Li, J.; Sun, Z.; He, K.; Cheng, H.M.; Li, F. The Rechargeable Aluminum Battery: Opportunities and Challenges. *Angew. Chem. Int. Ed.* **2019**, *58*, 11978–11996. [CrossRef]
14. Lin, M.C.; Gong, M.; Lu, B.; Wu, Y.; Wang, D.Y.; Guan, M.; Dai, H. An ultrafast rechargeable Aluminium-ion battery. *Nature* **2015**, *520*, 324–328. [CrossRef]
15. Liang, J.; Li, F.; Cheng, H.M. Metal ion storage: A route to versatile energy storage. *Energy Storage Mater.* **2018**, *11*, A1–A3. [CrossRef]
16. Ponrouch, A.; Bitenc, J.; Dominko, R.; Lindahl, N.; Johansson, P.; Palacin, M.R. Multivalent rechargeable batteries. *Energy Storage Mater.* **2019**, *20*, 253–262. [CrossRef]
17. Yoo, H.D.; Liang, Y.; Dong, H.; Lin, J.; Wang, H.; Liu, Y.; Ru, Q.; Jing, Y.; An, Q.; Zhou, W.; et al. Fast kinetics of magnesium monochloride cations in interlayer-expanded titanium disulfide for magnesium rechargeable batteries. *Nat. Commun.* **2017**, *8*, 339. [CrossRef]
18. Koketsu, T.; Giannini, M.; Ma, J.; Morgan, B.J.; Body, M.; Legein, C.; Dachraoui, W.; Demorterie, A.; Salanne, M.; Dardoize, F.; et al. Reversible magnesium and aluminium ions insertion in cation-deficient anatase TiO_2. *Nat. Mater.* **2017**, *16*, 1142–1148. [CrossRef]
19. Bonnick, P.; Muldoon, J. A Trip to Oz and a Peak Behind the Curtain of Magnesium Batteries. *Adv. Funct. Mater.* **2020**, *30*, 1910510. [CrossRef]
20. Deivanayagam, R.; Ingram, B.J.; Shahbazian-Yassar, R.S. Progress in development of electrolytes for magnesium batteries. *Energy Storage Mater.* **2019**, *21*, 136–153. [CrossRef]
21. Jung, K.H.; Jeong, G.S.; Go, C.Y.; Kim, K.C. Conjugacy of organic cathode materials for high-potential lithium-ion batteries: Carbonitriles versus quinones. *Energy Storage Mater.* **2020**, *24*, 237–246. [CrossRef]
22. Lu, D.; Liu, H.; Huang, T.; Xu, Z.; Ma, L.; Yang, P.; Qiang, P.; Zhang, F.; Wu, D. Magnesium ion based organic secondary batteries. *J. Mater. Chem. A Mater.* **2018**, *6*, 17297–17302. [CrossRef]
23. Cui, L.; Zhou, L.; Zhang, K.; Xiong, F.; Tan, S.; Li, M.; An, Q.; Kang, Y.M.; Mai, L. Salt-controlled dissolution in pigment cathode for high-capacity and long-life magnesium organic batteries. *Nano Energy* **2019**, *65*, 103902. [CrossRef]
24. Hu, P.; Wang, H.; Yang, Y.; Yang, J.; Lin, J.; Guo, L. Renewable-Biomolecule-Based Full Lithium-Ion Batteries. *Adv. Mater.* **2016**, *28*, 3486–3492. [CrossRef]
25. Lee, S.; Hong, J.; Jung, S.-K.; Ku, K.; Kwon, G.; Seong, W.M.; Kim, H.; Yoon, G.; Kang, I.; Hong, K.; et al. Charge-transfer complexes for high-power organic rechargeable batteries. *Energy Storage Mater.* **2019**, *20*, 462–469. [CrossRef]

26. Rodríguez-Pérez, I.A.; Yuan, Y.; Bommier, C.; Wang, X.; Ma, L.; Leonard, D.P.; Lerner, M.M.; Carter, R.G.; Wu, T.; Greaney, A.P.; et al. Mg-Ion Battery Electrode: An Organic Solid's Herringbone Structure Squeezed upon Mg-Ion Insertion. *J. Am. Chem. Soc.* **2017**, *139*, 13031–13037. [CrossRef]
27. Song, Z.; Zhou, H. Towards sustainable and versatile energy storage devices: An overview of organic electrode materials. *Energy Environ. Sci.* **2013**, *6*, 2280. [CrossRef]
28. Kumar, M.S.; Das, P.; Yasoda, K.Y.; Kothurkar, N.K.; Malik, S.; Batabyal, S.K. Fabrication of organic nanocomposite of polyaniline for enhanced electrochemical performance. *J. Energy Storage* **2020**, *31*, 101700. [CrossRef]
29. Han, C.; Li, H.; Shi, R.; Zhang, T.; Tong, J.; Li, J.Q.; Li, B. Organic quinones towards advanced electrochemical energy storage: Recent advances and challenges. *J. Mater. Chem. A Mater.* **2019**, *7*, 23378–23415. [CrossRef]
30. Nevers, D.R.; Brushett, F.R.; Wheeler, D.R. Engineering radical polymer electrodes for electrochemical energy storage. *J. Power Sources* **2017**, *352*, 226–244. [CrossRef]
31. Senoh, H.; Yao, M.; Sakaebe, H.; Yasuda, K.; Siroma, Z. A two-compartment cell for using soluble benzoquinone derivatives as active materials in lithium secondary batteries. *Electrochim. Acta* **2011**, *56*, 10145–10150. [CrossRef]
32. Williams, D.L.; Byrne, J.; Driscoll, J.S. A High Energy Density Lithium/Dichloroisocyanuric Acid Battery System. *J. Electrochem. Soc.* **1969**, *116*, 2. [CrossRef]
33. Vedhanarayanan, B.; Huang, T.H.; Lin, T.W. Fabrication of 3D hierarchically structured carbon electrode for supercapacitors by carbonization of polyaniline/carbon nanotube/graphene composites. *Inorg. Chim. Acta* **2019**, *489*, 217–223. [CrossRef]
34. Kumar, M.S.; Yasoda, K.Y.; Batabyal, S.K.; Kothurkar, N.K. Carbon-polyaniline nanocomposites as supercapacitor materials. *Mater. Res. Express* **2018**, *5*, 045505. [CrossRef]
35. Lu, M.N.; Dai, C.S.; Tai, S.Y.; Lin, T.W.; Lin, J.Y. Hierarchical nickel sulfide/carbon nanotube nanocomposite as a catalytic material toward triiodine reduction in dye-sensitized solar cells. *J. Power Sources* **2014**, *270*, 499–505. [CrossRef]
36. Yasoda, K.Y.; Kumar, S.; Kumar, M.S.; Ghosh, K.; Batabyal, S.K. Fabrication of MnS/GO/PANI nanocomposites on a highly conducting graphite electrode for supercapacitor application. *Mater. Today Chem.* **2021**, *19*, 100394. [CrossRef]
37. Yamada, Y.; Wang, J.; Ko, S.; Watanabe, E.; Yamada, A. Advances and issues in developing salt-concentrated battery electrolytes. *Nat. Energy* **2019**, *4*, 269–280. [CrossRef]
38. Wang, Y.; Meng, X.; Sun, J.; Liu, Y.; Hou, L. Recent Progress in 'Water-in-Salt' Electrolytes Toward Non-lithium Based Rechargeable Batteries. *Front. Chem.* **2020**, *8*, 595. [CrossRef]
39. Park, J.; Lee, J.; Kim, W. Water-in-Salt Electrolyte Enables Ultrafast Supercapacitors for AC Line Filtering. *ACS Energy Lett.* **2021**, *6*, 769–777. [CrossRef]
40. Xiao, D.; Zhang, L.; Li, Z.; Dou, H.; Zhang, X. Design strategies and research progress for Water-in-Salt electrolytes. *Energy Storage Mater.* **2022**, *44*, 10–28. [CrossRef]
41. Cao, J.; Su, E. Hydrophobic deep eutectic solvents: The new generation of green solvents for diversified and colorful applications in green chemistry. *J. Clean. Prod.* **2021**, *314*, 127965. [CrossRef]
42. Cruz, H.; Jordão, N.; Branco, L.C. Deep eutectic solvents (DESs) as low-cost and green electrolytes for electrochromic devices. *Green Chem.* **2017**, *19*, 1653–1658. [CrossRef]
43. Smith, E.L.; Abbott, A.P.; Ryder, K.S. Deep Eutectic Solvents (DESs) and Their Applications. *Chem. Rev.* **2014**, *114*, 11060–11082. [CrossRef] [PubMed]
44. Zhang, C.; Zhang, L.; Yu, G. Eutectic Electrolytes as a Promising Platform for Next-Generation Electrochemical Energy Storage. *Acc Chem. Res.* **2020**, *18*, 1648–1659. [CrossRef] [PubMed]
45. Tsai, H.H.; Lin, T.J.; Vedhanarayanan, B.; Tsai, C.C.; Chen, T.Y.; Lin, T.W. A 1.9-V all-organic battery-supercapacitor hybrid device with high-rate capability and wide temperature tolerance in a metal-free water-in-salt electrolyte. *J. Colloid. Interface Sci.* **2022**, *612*, 76–87. [CrossRef]
46. Du, C.; Zhao, B.; Chen, X.B.; Birbilis, N.; Yang, H. Effect of water presence on choline chloride-2urea ionic liquid and coating platings from the hydrated ionic liquid. *Sci. Rep.* **2016**, *6*, 29225. [CrossRef]
47. Bo, Z.; Zhou, M.; Zhou, S.; Song, Y.; Liu, Z.; Liao, H.; Yang, H.; Yan, J.; Cen, K.; Fan, X.; et al. Controlling Interfacial Structural Evolution in Aqueous Electrolyte via Anti-Electrolytic Zwitterionic Waterproofing. *Adv. Funct. Mater.* **2022**, *32*, 202207140. [CrossRef]
48. Khan, M.; Khan, K.; Hemant, S.; Kumar, M.; Gupta, K. Detection of Urea Adulteration in Milk Using Near-Infrared Raman Spectroscopy. *Food Anal. Methods* **2014**, *8*, 93–102. [CrossRef]
49. Hu, Y.; Wang, Z.; Huang, X.; Chen, L. Physical and electrochemical properties of new binary room-temperature molten salt electrolyte based on LiBETI and acetamide. *Solid State Ion.* **2004**, *175*, 277–280. [CrossRef]
50. Hu, Y.; Wang, Z.; Li, H.; Huang, X.; Chen, L. Spectroscopic studies on the mechanism of liquid formation and ionic conductivity in the $LiCF_3SO_3$/acetamide complex system. *Vib. Spectrosc.* **2005**, *37*, 1–10. [CrossRef]
51. Wu, X.; Qi, Y.; Hong, J.J.; Li, Z.; Hernandez, A.S.; Ji, X. Rocking-Chair Ammonium-Ion Battery: A Highly Reversible Aqueous Energy Storage System. *Angew. Chem.* **2017**, *129*, 13206–13210. [CrossRef]
52. Lei, X.; Zheng, Y.; Zhang, F.; Wang, Y.; Tang, Y. Highly stable magnesium-ion-based dual-ion batteries based on insoluble small-molecule organic anode material. *Energy Storage Mater.* **2020**, *30*, 34–41. [CrossRef]
53. Wang, J.; Polleux, J.; Lim, J.; Dunn, B. Pseudocapacitive contributions to electrochemical energy storage in TiO_2 (anatase) nanoparticles. *J. Phys. Chem. C* **2007**, *111*, 14925–14931. [CrossRef]

54. Guo, Z.; Chen, L.; Wang, Y.G.; Wang, C.; Xia, Y. Aqueous Lithium-Ion Batteries Using Polyimide-Activated Carbon Composites Anode and Spinel $LiMn_2O_4$ Cathode. *ACS Sustain. Chem. Eng.* **2017**, *5*, 1503–1508. [CrossRef]
55. Gavilán-Arriazu, E.M.; Mercer, M.P.; Pinto, O.A.; Oviedo, O.A.; Barraco, D.E.; Hoster, H.E.; Leiva, E.P.M. Numerical simulations of cyclic voltammetry for lithium-ion intercalation in nanosized systems: Finiteness of diffusion versus electrode kinetics. *J. Solid State Electrochem.* **2020**, *24*, 3279–3287. [CrossRef]
56. Zhang, Z.; Li, Y.; Zhao, G.; Zhu, L.; Sun, Y.; Besanbacher, F.; Yu, M. Rechargeable Mg-Ion Full Battery System with High Capacity and High Rate. *ACS Appl. Mater. Interfaces* **2021**, *13*, 40451–40459. [CrossRef]
57. Wen, Y.; Ma, C.; Chen, H.; Zhang, H.; Li, M.; Zhao, P.; Qiu, J.; Ming, H.; Cao, G.; Tang, G. Stabilizing $LiMn_2O_4$ cathode in aqueous electrolyte with optimal concentration and components. *Electrochim. Acta* **2020**, *362*, 137079. [CrossRef]
58. Wang, Y.; Chen, L.; Wang, Y.; Xia, Y. Cycling Stability of Spinel $LiMn_2O_4$ with Different Particle Sizes in Aqueous Electrolyte. *Electrochim. Acta* **2015**, *173*, 178–183. [CrossRef]
59. Wang, F.; Fan, X.; Gao, T.; Sun, W.; Ma, Z.; Yang, C.; Han, F.; Xu, K.; Wang, C. High-Voltage Aqueous Magnesium Ion Batteries. *ACS Cent. Sci.* **2017**, *3*, 1121–1128. [CrossRef]
60. Chen, L.; Bao, J.L.; Dong, X.; Truhlar, D.G.; Wang, Y.; Wang, C.; Xia, Y. Aqueous Mg-ion battery based on polyimide anode and prussian blue cathode. *ACS Energy Lett.* **2017**, *2*, 1115–1121. [CrossRef]
61. Mizuno, Y.; Okubo, M.; Hosona, E.; Kudo, T.; Oh-Ishi, K.; Okazawa, A.; Kojima, N.; Kurona, R.; Nishimura, N.I.; Yamada, A. Electrochemical Mg2+ intercalation into a bimetallic CuFe Prussian blue analog in aqueous electrolytes. *J. Mater. Chem. A Mater.* **2013**, *1*, 13055–13059. [CrossRef]
62. Zhang, H.; Ye, K.; Zhu, K.; Cang, R.; Yan, J.; Cheng, K.; Wang, G.; Cao, D. Aqueous Magnesium-Ion Battery Based on a Carbon-Coated FeVO4 Anode and a Mg-OMS-1 Cathode. *Chem.—A Eur. J.* **2017**, *23*, 17118–17126. [CrossRef] [PubMed]
63. Huang, Z.D.; Masese, T.; Orikasa, Y.; Mori, T.; Minato, T.; Tassel, C.; Kobayashi, Y.; Kageyama, H.; Uchimoto, Y. MgFePO4F as a feasible cathode material for magnesium batteries. *J. Mater. Chem. A Mater.* **2014**, *2*, 11578–11582. [CrossRef]
64. Zhang, H.; Ye, K.; Zhu, K.; Cang, R.; Wang, X.; Wang, G.; Cao, D. Assembly of Aqueous Rechargeable Magnesium Ions Battery Capacitor: The Nanowire Mg-OMS-2/Graphene as Cathode and Activated Carbon as Anode. *ACS Sustain. Chem. Eng.* **2017**, *5*, 6727–6735. [CrossRef]

Disclaimer/Publisher's Note: The statements, opinions and data contained in all publications are solely those of the individual author(s) and contributor(s) and not of MDPI and/or the editor(s). MDPI and/or the editor(s) disclaim responsibility for any injury to people or property resulting from any ideas, methods, instructions or products referred to in the content.